Tectonic inheritance during plate boundary evolution in southern California constrained from seismic anisotropy
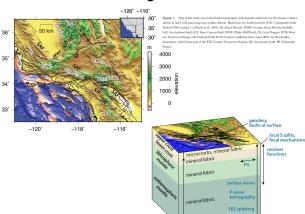
Thorsten W. Becker[1], Vera Schulte-Pelkum[2], Whitney M. Behr[3], and Meghan S. Miller[4]

[1]UT Austin (twb@ig.utexas.edu), [2]CU Boulder, [3]ETH Zurich, [4]RES, ANU Canberra

2021 SCEC Annual Meeting, Poster #113

Abstract

The style of convective force transmission to plates and strain-localization within and underneath plate boundaries remain debated. To address some of the related issues, we analyze a range of deformation indicators in southern California from the surface to the asthenosphere. Present-day surface strain rates can be inferred from geodesy. At seismogenic crustal depths, stress can be inferred from focal mechanisms and splitting of shear waves from local earthquakes via crack-dependent seismic velocities. At greater depths, constraints on rock fabrics are obtained from receiver function anisotropy, Pn and P tomography, surface wave tomography, and splitting of SKS and other teleseismic core phases. We construct a synthesis of deformation-related observations focusing on quantitative comparisons of deformation style. We find consistency with roughly N-S compression and E-W extension near the surface and in the asthenospheric mantle. However, all lithospheric anisotropy indicators show deviations from this pattern. Pn fast axes and dipping foliations from receiver functions are fault-parallel with no localization to fault traces and match post-Farallon block rotations in the Western Transverse Ranges. Local shear wave splitting orientations deviate from the stress orientations inferred from focal mechanisms in significant portions of the area. We interpret these observations as an indication that lithospheric fabric, developed during Farallon subduction and subsequent extension, has not been completely reset by present-day transform motion and may influence the current deformation behavior. This provides a new perspective on the timescales of deformation memory and lithosphere-asthenosphere interactions.
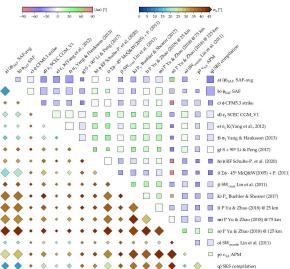
Background

Figure 1. Map of the study area with shaded topography and elements referred to in text (larger context shown in inset with main map area outline drawn). Black lines are faults from the SCEC Community Fault Model (CFM) version 1.5 (Plesch et al., 2007), SN: Sierra Nevada; WSNF: western Sierra Nevada foothills; SAF: San Andreas Fault; KCF: Kern Canyon Fault; WWF: White Wolf Fault; CR: Coast Ranges; WTR: Western Transverse Ranges; GF: Garlock Fault; ECSZ: Eastern California shear zone; SBM: San Bernardino Mountains, which form part of the ETR: Eastern Transverse Ranges; SJF: San Jacinto Fault; PB: Peninsular Ranges.

Figure 2. Perspective view of the study area with elevation and topography (surface color) and fault traces. Vertical dimension shows conceptual sketch of observables (blue) and their depth sensitivities (arrows) as well as presumed mechanisms (italic script) that may dominate azimuthally varying observations in different depth layers (color).

Overview of results

Results

Figure 3. (a) Fast axis orientation and delay time of SKS splits (compilation of Becker et al., 2012, updated as of 2020) and Rayleigh wave upper mantle fast axis and percent anisotropy (orange bars; Lin et al., 2011). Elevation shading and faults are shown for orientation, with faults in green for surface traces and red for blind faults from the SCEC CFM5.3 as in Fig. 1. (b) Signed angular difference comparison between the two orientation sets (color coding of bars in angle sign definition as in (a); amplitude information is not used in this case). Inset shows histogram of the angular differences, with mean(median) and standard deviation indicated; N is number of measurements pairs per bin, N0 total number of pairs.
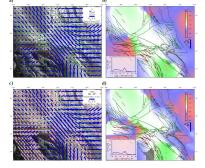

Figure 5. (a) In blue, fast propagation axes and % anisotropy from Pn tomography (Buehler & Shearer, 2017), compared to SAF strike averaged outside of the Big Bend (green bars). (b) Signed angular difference of the quantities in (a), description as For Fig. 3b. (c) Pn as in (a), but here compared to Farallon convergence-perpendicular strike including subsequent block rotations from McQuarrie and Wernicke (2005) with interpolated values from Porter et al. (2011). (d) Misorientation for (c), description as in Fig. 3b.

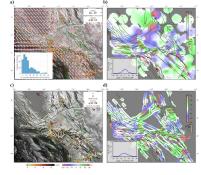**Figure 6.** (a) Strikes and amplitude of largest A1 harmonic receiver function arrival at each station (in orange), compared to Farallon paleofabric (in pink) as in Fig. 5c). Inset shows depth distribution of A1 arrivals. (b) Orientation comparison for (a) as in Fig. 3b. (c) As in (a), but here compared to local fault strikes from SCEC CFM 5.3 (Plesch et al., 2007) and colored by conversion depth. Short arrows show receiver function inferred up-or downdip direction, colored by the strike of that vector to allow easier geographic subsetting. (d) Orientation comparison for (c).

Figure 4. Mean angular difference (squares, scaled by "unimodality", i.e. unity minus Sarle's bimodality coefficient, $1 - \frac{s^2+1}{\kappa}$ where γ and κ are the skewness and kurtosis, respectively) and standard deviation of the distribution (diamonds, scaled by the coverage area, cf. Fig. 9) for an extended selection of data sets. a) Mean SAF fault strike (single value); b) SAF fault strike perpendicularly extended from the main fault (both from the Pacific-North America plate boundary from Bird, 2003); c) local fault strike from SCEC CFM 5.3 (Plesch et al., 2007) (cf. Fig. 6); d) extensional axes from SCEC CGM_V1 (Sandwell et al., 2016) geodetic strain rates (cf. Fig. 7); e) extensional axes of a Kostrov summation of an update of the Yang et al. (2012) focal mechanisms; f) extensional stress from Yang et al. (2012) based stress inversion (Yang & Hauksson, 2013) (cf. Fig. 7); g) fast axes from local S splits (Z. Li & Peng, 2017) plus 90°; h) fast axes from receiver functions (Schulte-Pelkum, Ross, et al., 2020) (cf. Fig. 6); i) cumulative block rotations from McQuarrie and Wernicke (2005) and Porter et al. (2011) minus 45° (cf. Fig. 5); j) crustal-depth surface wave anisotropy (Lin et al., 2011); k) Pn anisotropy (Buehler & Shearer, 2017) (cf. Fig. 5); k-n) P tomography fast axes (Yu & Zhao, 2018) at depths of 25, 75, and 125 km, respectively; o) mantle depth surface wave anisotropy (Lin et al., 2011) (cf. Fig. 3); p) absolute plate motion (APM) orientations in the spreading-aligned reference frame (Becker et al., 2015); and q) SKS splitting compilation fast axes (update of Becker et al., 2012) (cf. Fig. 3). Clicking on any of the symbols in the PDF version of this article provides a link to web based cross-comparison plots such as in Fig. 3. (To be implemented: For now, the reader can access all the plots from, e.g., http://www-udc.ig.utexas.edu/external/becker/vwus/wusan.c-d.png, where "c" and "d" are referring to the models as per the figure legend.)
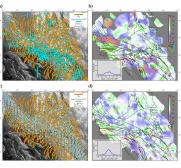

Figure 7. (a) Compressive stress from focal mechanism inversion in orange (Yang & Hauksson, 2013) compared to local event S splitting fast axes (Z. Li & Peng, 2017) in cyan. (b) Orientation comparison for (a) as in Fig. 3b. (c) Focal mechanism compressive stress axes (in orange) as in (a), here with compressive strain-rate axes from the Southern California Earthquake Center (in light blue) (SCEC) CGM_V1 (Sandwell et al., 2016), scaled with maximum shear strain amplitude. (d) Orientation comparison for (c).

Figure 9. Angular difference histograms ($-90 \ldots 90°$) as in e.g. Fig 3b for all data sets discussed above. The top right triangle has as diamonds the median deviation, with the diamond's size scaled by the inverse of the standard deviation and the diamond centered on the median. The lower left has the same coloring, but the square size scales with the area of coverage out of the whole study area. See Fig. 4 for abbreviated representation of an extended comparison set.
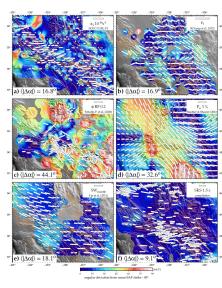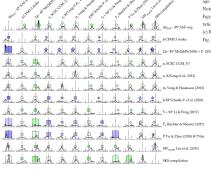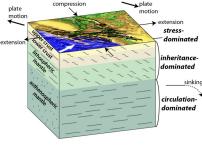

Figure 8. Comparison of six data sets in a common reference system. The reference orientation is average SAF strike rotated 45° counterclockwise to match approximate SKS and surface extension orientations. Note that the background color scale used to represent axis misorientation is different from that used in Figs. 3-7; purple/blue shades now show alignment, and we do not distinguish between CW and CCW rotations, i.e. $|\Delta\alpha| \in [0; 90°]$. (a) GPS extension as in Fig. 7c. (b) focal mechanism extension as in Fig. 7a,c. (c) Receiver function strikes as in Fig. 6. (d) Pn fast axis as in Fig. 5. (e) Mantle surface wave fast axis as in Fig. 3. (d) SKS fast axes as in Fig. 3.

Conclusions

We compare orientations of stress- and deformation-associated observables such as surface deformation, stress state inverted from focal mechanisms, local event and teleseismic shear wave splitting, receiver function inferred azimuthally varying conversions, Pn and local/teleseismic P tomography, and surface wave azimuthal anisotropy, in addition to geological information such as fault strike and block rotations since Farallon subduction. The deformation indicators separate into three classes, with a near-surface match between geodesy and focal mechanisms and some local event shear wave splits, a lithospheric depth range comprising receiver functions, Pn, and local event splitting in other areas, and an asthenospheric component detected by mantle surface waves and SKS splitting that is driven by mantle circulation and can be speculated to transmit through the lithosphere to drive stress at the surface. Notably, lithospheric rock fabric and anisotropy do not appear to be reset to reflect present-day deformation and instead appear to persist since the time of accretion and intrusion during long-lived subduction. Fabric from the upper crust through the lithospheric mantle appears to have been preserved and rotated along with surface block rotations through temporal changes in deformation regimes.
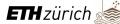
References

Much of this poster is discussed in a submitted article, with a preprint including all references to the original work at:
Schulte-Pelkum, V., Becker, T. W., Behr, W. M., and Miller, M. S.: Tectonic inheritance during plate boundary evolution in southern California constrained from seismic anisotropy, *Earth and Space Science Open Archive*, doi: 10.1002/essoar.10507775.1, 2021.

Acknowledgments